Supporting Information for "Local-scale secondary water inputs modulate seasonal vegetation cover decay rate across Africa"

Çağlar Küçük [1,2], Sujan Koirala [1], Nuno Carvalhais [1,3], Diego G. Miralles [2],

Markus Reichstein [1], Martin Jung [1]

[1]Department of Biogeochemical Integration, Max Planck Institute for Biogeochemistry, Jena, Germany

[2]Hydro-Climate Extremes Lab (H-CEL), Faculty of Bioscience Engineering, Ghent University, Ghent, Belgium

[3]CENSE, Departamento de Ciências e Engenharia do Ambiente, Faculdade de Ciências e Tecnologia, Universidade NOVA de Lisboa, Caparica, Portugal

Contents of this file

Detailed description of the data

In this section, details of the data used in this study are given, such as the methods for spatial and temporal aggregation, as well as the details of estimated parameters separately for land, climate and vegetation.

Land:

We used three sets of predictors to model land effects which covers soil hydraulic properties, water table depth and topographic complexity. In order to prepare the first set of predictors, we used sand, clay and organic matter contents of soil, together with volumetric coarse fragments data from SoilGrids dataset (Hengl et al., 2017) for top and deep soil. We grouped layers up to 1 meter as top soil and the rest as deep soil and finally took mean of the layers. We then calculated soil hydraulic properties using the equations in Saxton and Rawls (2006). Additionally, we estimated maximum potential upwards capillary flux (I_{cap}) in millimetres per day (mm/day) at 1 meter above groundwater level using Richards' equation (Richards, 1931). Finally, we used Plant Available Water (PAW) as the difference in soil water content between field capacity and wilting point, soil hydraulic conductivity at field capacity (k_{FC}) and I_{cap} for two layers as predictors to model λ. SoilGrids dataset was aggregated to target resolution by taking mean.

We defined the second set of predictors considering Water Table Depth (WTD). Additional to the WTD data from Fan, Li, and Miguez-Macho (2013), we also used Height Above Nearest Drainage (HAND) data from Yamazaki et al. (2019) since HAND is a good proxy to show the drainage positions (Fan et al., 2019), which strongly affect the depth of groundwater. We aggregated WTD and HAND by taking mean. Even though seasonal

variations of WTD may be significant, WTD product used in this study is static due to properties of high resolution products. In order to capture effects of seasonally shallow groundwater, i.e., due to seasonal flooding, we used the wetlands data from Tootchi, Jost, and Ducharne (2019). We aggregated the data by computing percentage of wetlands over target grid cells.

Last set of land predictors used for modelling λ is related to topographic complexity. We used Topographic Wetness Index (TWI) as a proxy for the likelihood of soil moisture due to lateral convergence. In order to account for slope and aspect at hillslope scales, we used Vectoral Ruggedness Measure (VRM) which is a compound metric quantifying slope and aspect together using a sine-cosine derivation. Overall VRM values, having a range from 0 to 1, increase with ruggedness. Finally, we used magnitude and scale of terrain roughness, which is derived from VRM. Magnitude of roughness is an important parameter to represent the variation in topography even after spatial aggregation. All data used in this set of predictors are obtained from Amatulli, McInerney, Sethi, Strobl, and Domisch (2020) and aggregated by taking the mean.

Climate:

We used mean values for temperature and radiation, and total precipitation for annual time scales. For seasonal scales, we used seasonality and annual range of temperature and precipitation that are available in monthly resolution from Fick and Hijmans (2017) in the native spatial resolution of λ. For radiation, we computed the features from the monthly data of Abatzoglou, Dobrowski, Parks, and Hegewisch (2018), with the same approach taken for temperature.

Vegetation:

We used canopy height from Simard, Pinto, Fisher, and Baccini (2011) after aggregating the original data to 5 km resolution by mean. Additionally, we used four MODIS based products which are vegetation cover for both tree and non-tree fractions (Dimiceli et al., 2015), burned area (Giglio et al., 2015) and Plant Functional Type (PFT) (Friedl & Sulla-Menashe, 2019). While the first three are aggregated by taking mean values within the target grid cell, PFT is aggregated by assigning the most common class found within the grid cell. Additional to the major type of PFT within grid cell, we computed Shannon's diversity index (Shannon, 1948) of the PFTs within the grid cells to be aggregated and used as another predictor.

Spatial distribution of the target variable

Spatial distribution of the target variable is shown in Fig. S1. Yellow colour represents faster rate of seasonal vegetation cover decay while blue represents slower decay. Note that study domain is filtered based on the quality of λ estimations and annual precipitation of 1500 mm/year. Further details of the metric and its derivation is available in Küçük et al. (2020).

Land attributed variations in λ

In this section, we present the land attributed variations of λ using the raw SHAP values of the modelled λ. Spatial variation of the raw SHAP values are given in Fig. S2 as total attribution, together with it's component as direct land effects and land interaction effects with climate and vegetation in the panels. Directly land attributed variations ($\phi_{land-direct}$) are the dominant component of the total land attributed variations of λ ($\phi_{land-total}$). Large

positive values in $\phi_{land-direct}$ in regions with shallow groundwater like the Sudd Swamp (Box-D) where groundwater is shallow (Tootchi et al., 2019) and with complex topography like the Ethiopian Highlands (Box-E) show that the e-folding time of FVC is slowed down up to 6 days directly owing to the land parameters modulating secondary water resources – see Fig. S2a. Conversely, we observed strong negative effects in very arid regions like Senegal (Box-A in Fig. S2b), Somalia, and the Kalahari Desert, where groundwater is disconnected from surface (Fan et al., 2013).

Interestingly, interaction effects between land and climate make strong positive variation on λ in Okavango Delta (Box-C in Fig. S2c) that inverts the negative effects of land parameters in the region. This conceptually agrees with the fact that the Okavango Delta, being a seasonally flooded delta, is strongly affected by climate seasonality (Cronberg et al., 1995). Lastly, interaction effects between land and vegetation are not so prominent through the study domain (Fig. S2d).

Climate and vegetation attributed variations in λ

Spatial variations of raw SHAP values for climate and vegetation are given in Fig. S3 to illustrate their effects on λ as direct effects ($\phi_{clim-direct}$ and $\phi_{veg-direct}$) and interaction effects ($\phi_{clim-veg}$).

References

Abatzoglou, J. T., Dobrowski, S. Z., Parks, S. A., & Hegewisch, K. C. (2018). TerraClimate, a high-resolution global dataset of monthly climate and climatic water balance from 1958-2015. *Scientific Data*, *5*, 1–12. doi: 10.1038/sdata.2017.191

Amatulli, G., McInerney, D., Sethi, T., Strobl, P., & Domisch, S. (2020). Geomorpho90m, empirical evaluation and accuracy assessment of global high-resolution geomorphometric layers. *Scientific Data*, *7*(1), 1–18. doi: 10.1038/s41597-020-0479-6

Cronberg, G., Gieske, A., Martins, E., Prince Nengu, J., & Stenström, I.-M. (1995). Hydrobiological studies of the Okavango Delta and Kwando/Linyati/Chobe River, Botswana I surface water quality analysis. *Botswana Notes and Records*, *27*. Retrieved from `http://www.jstor.org/stable/40980045`

Dimiceli, C., Carroll, M., Sohlberg, R., Kim, D. H., Kelly, M., & Townshend, J. R. G. (2015). *MOD44B MODIS/Terra Vegetation Continuous Fields Yearly L3 Global 250m SIN Grid V006.* NASA EOSDIS Land Processes DAAC. doi: 10.5067/MODIS/MOD44B.006

Fan, Y., Clark, M., Lawrence, D. M., Swenson, S., Band, L. E., Brantley, S. L., ... Yamazaki, D. (2019). Hillslope hydrology in global change research and earth system modeling. *Water Resources Research*, 1737–1772. doi: 10.1029/2018WR023903

Fan, Y., Li, H., & Miguez-Macho, G. (2013). Global patterns of groundwater table depth. *Science*, *339*(6122), 940–943. doi: 10.1126/science.1229881

Fick, S. E., & Hijmans, R. J. (2017). WorldClim 2: new 1-km spatial resolution climate surfaces for global land areas. *International Journal of Climatology*, *37*(12), 4302–

4315. doi: 10.1002/joc.5086

Friedl, M., & Sulla-Menashe, D. (2019). *MCD12Q1 MODIS/Terra+Aqua Land Cover Type Yearly L3 Global 500m SIN Grid V006.* NASA EOSDIS Land Processes DAAC. doi: 10.5067/MODIS/MCD12Q1.006

Giglio, L., Justice, C., Boschetti, L., & Roy, D. (2015). *MCD64A1 MODIS/Terra+Aqua Burned Area Monthly L3 Global 500m SIN Grid V006.* NASA EOSDIS Land Processes DAAC. doi: 10.5067/MODIS/MCD64A1.006

Hengl, T., Mendes de Jesus, J., Heuvelink, G. B., Gonzalez, M. R., Kilibarda, M., Blagotić, A., ... Kempen, B. (2017). SoilGrids250m: Global gridded soil information based on machine learning. *PLoS ONE*, *12*(2), 1–40. doi: 10.1371/journal.pone.0169748

Küçük, Ç., Koirala, S., Carvalhais, N., Miralles, D. G., Reichstein, M., & Jung, M. (2020). Characterising the response of vegetation cover to water limitation in Africa using geostationary satellites. *Earth and Space Science Open Archive*, 38. doi: 10.1002/essoar.10504964.2

Richards, L. A. (1931). Capillary conduction of liquids through porous mediums. *Journal of Applied Physics*, *1*(5), 318–333. doi: 10.1063/1.1745010

Saxton, K. E., & Rawls, W. J. (2006). Soil Water Characteristic Estimates by Texture and Organic Matter for Hydrologic Solutions. *Soil Science Society of America Journal*, *70*(5), 1569–1578. doi: 10.2136/sssaj2005.0117

Shannon, C. E. (1948). A mathematical theory of communication. *The Bell System Technical Journal*, *27*(3), 379-423. doi: 10.1002/j.1538-7305.1948.tb01338.x

Simard, M., Pinto, N., Fisher, J. B., & Baccini, A. (2011). Mapping forest canopy height globally with spaceborne lidar. *Journal of Geophysical Research: Biogeosciences*, *116*(4), 1–12. doi: 10.1029/2011JG001708

Tootchi, A., Jost, A., & Ducharne, A. (2019). Multi-source global wetland maps combining surface water imagery and groundwater constraints. *Earth System Science Data*, *892657*, 189–220. doi: 10.5194/essd-11-189-2019

Yamazaki, D., Ikeshima, D., Sosa, J., Bates, P. D., Allen, G. H., & Pavelsky, T. M. (2019). MERIT Hydro: A High-Resolution Global Hydrography Map Based on Latest Topography Dataset. *Water Resources Research*, *55*(6), 5053–5073. doi: 10.1029/2019WR024873

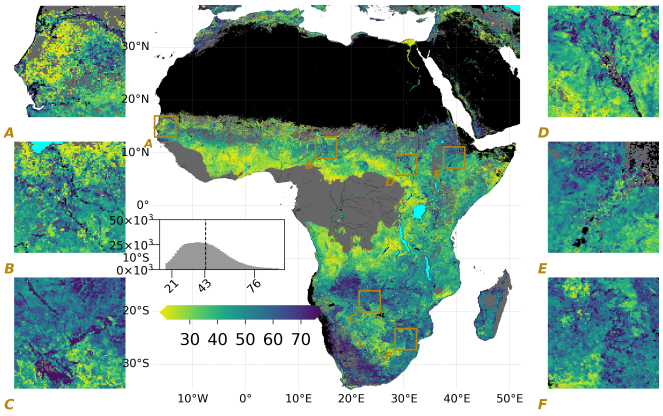

Figure S1. Observed λ as the target variable of the gradient boosting model.

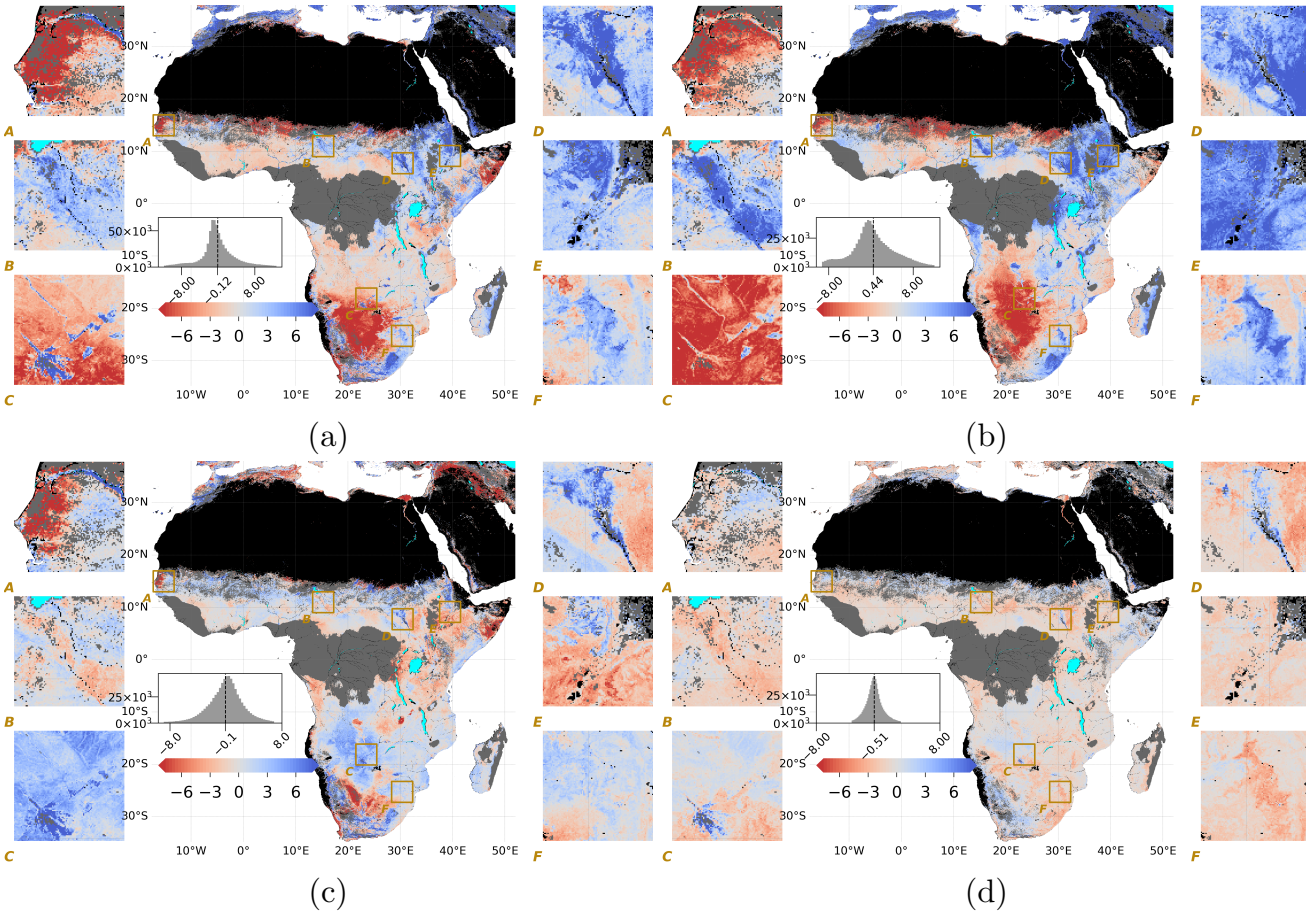

Figure S2. Land attributed variations of λ as (a) total effects, $\phi_{land-total} = \phi_{land-direct} + \phi_{land-clim} + \phi_{land-veg}$, (b) direct effects of land, $\phi_{land-direct}$, (c) interaction effects between land and climate, $\phi_{land-clim}$, (d) interaction effects between land and vegetation, $\phi_{land-veg}$.

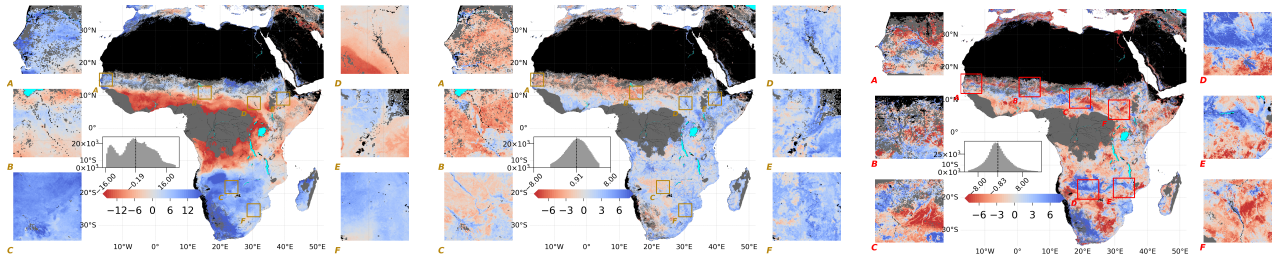

(a) (b) (c)

Figure S3. Maps of feature attribution for (a) direct effects of climate ($\phi_{clim-direct}$), (b) direct effect of vegetation ($\phi_{veg-direct}$), (c) interaction effects between climate and vegetation ($\phi_{clim-veg}$). Note the larger range of colourbar in $\phi_{clim-direct}$ than other maps of raw SHAP values.